INORGANIC CHEMISTRY
FRONTIERS

RESEARCH ARTICLE

View Article Online
View Journal | View Issue

Cite this: *Inorg. Chem. Front.*, 2026, **13**, 341

Spin state modulation and chiral hierarchical assembly *via* amine-driven single-crystal-to-single-crystal transformation

Xu Ying,[a] Zhenhua Zhu, *[a] Peng Xu,[a,b] Quan Zhou[a,b] and Jinkui Tang *[a,b]

Received 30th August 2025,
Accepted 19th October 2025

DOI: 10.1039/d5qi01812a

rsc.li/frontiers-inorganic

We report a mononuclear Fe(II) synthon, **Fe-BF$_4$**, with four acidic NH sites and two terminal iodo-groups, for achieving achiral or chiral supramolecular hydrogen- and/or halogen-bond frameworks through amine-driven single-crystal-to-single-crystal (SC–SC) transformation. Et$_3$N-driven SC–SC transformation enables the formation of both a hydrogen- and halogen-bonded 2D architecture and a halogen-bonded 1D chain, accompanied by a magnetic transition from spin-crossover behavior to the low-spin state. When the optically pure amine, *R*/*S*-quinuclidinol, is introduced, the crystal undergoes a transformation from a centrosymmetric to a chiral structure. This successfully generates 1D hydrogen-bonded helical chains with M/P-helicity, which are further orthogonally linked *via* intermolecular C–I···N halogen bonds, forming three individual yet identical networks. Remarkably, these three networks adopt an alternating stacking arrangement, resulting in a three-fold interpenetrated supramolecular architecture. This hierarchical assembly illustrates a controlled transition from an achiral to a chiral configuration. Therefore, the amine-triggered SC–SC transformation in **Fe-BF$_4$** provides an effective strategy for simultaneously controlling the topological architectures and spin states of advanced supramolecular frameworks.

Introduction

Single-crystal-to-single-crystal (SC–SC) transformation has attracted enormous interest in crystal engineering as it provides an ideal method to modulate physicochemical properties of materials, showing great potential in porous materials,[1,2] molecular magnetism and ferroelectricity,[3–5] and molecular actuators.[6,7] At the molecular level, such transformations induced by light, heat, solvent exchange and static pressure are vital in accurately understanding structure–property–function relationships.[8–10] For example, SC–SC isomerization allowed *ab initio* calculations for a 1D photochromic dysprosium single-molecule magnet (SMM) before and after visible irradiation, thereby enabling the elucidation of the relaxation mechanism of magnetization in closed and open isomers.[11] In addition, SC–SC transformation is a kind of a topochemical synthesis strategy, presenting great advantages in creating novel functional crystalline materials with attractive chiroptical properties, spin-crossover (SCO) behaviors and ferroelectricity.[12–18] However, the number of examples of SC–SC transformation still remains limited as it is usually difficult to retain crystallinity after being subjected to an external stimulation or post-chemical modification, especially in 0D metal coordination complexes.[19] In 2014, Aromí *et al.* reported a heteroleptic 0D low-spin Fe(II) complex, [Fe(bpp)(H$_2$L$_1$)](ClO$_4$)$_2$·1.5C$_3$H$_6$O (bpp = 2,6-bis(pyrazol-3-yl)pyridine, H$_2$L$_1$ = 2,6-bis(5-(2-methoxyphenyl)pyrazol-3-yl)pyridine),[20] which showed a three-way SC–SC transformation *via* absorption, desorption and exchange of small solvent molecules, achieving the full conversion cycle of spin states by virtue of the fact that SCO behavior is highly sensitive to subtle structural changes.[20–23] In 2018, Zheng *et al.* achieved a reversible SC–SC transformation in a mononuclear Dy(III) complex, Dy(depma)(NO$_3$)$_3$(hmpa)$_2$ (depma = 9-diethylphosphono-methylanthracene, hmpa = hexamethylphosphoramide), *via* the intermolecular dimerization and de-dimerization between two neighboring anthracene units.[24] Such transformations lead to profound changes in magnetization dynamics and luminescent properties before and after photodimerization, paving a new way to construct magneto-optical smart materials. In addition, the SC–SC transformation of a 0D metal coordination complex can induce chiral interconversions, as exemplified by the simple centrosymmetric [Zn(eg)$_3$]SO$_4$ (eg = ethylene glycol) complex reported by Tao *et al.*[17] When the crystal was heated, it eliminated eg *via* a two-step thermal elimination process, along with preserving its crystallinity, leading to

[a]*State Key Laboratory of Rare Earth Resource Utilization, Changchun Institute of Applied Chemistry, Chinese Academy of Sciences, Changchun 130022, P. R. China. E-mail: tang@ciac.ac.cn, zhuzh@ciac.ac.cn*
[b]*School of Applied Chemistry and Engineering, University of Science and Technology of China, Hefei 230026, P. R. China*

changes in topological structures and molecule symmetries, *i.e.* from 0D to 1D to 3D accompanied by a centric-chiral-polar symmetric variation.

Apart from the above solvent-, light- and thermal-responsive molecule-based metal complexes, acid–base-responsive species for intelligent molecular devices have sparked great interest in recent years. In general, they possess acidic protons in the prototype compound and show reversible deprotonation/protonation behavior.[25–27] More interestingly, the number of acidic protons can be controlled chemically, providing a unique chance to precisely modulate the quantum states and magneto-optical properties of materials.[28] In 2019, Shiga *et al.* reported a mononuclear homoligand Fe(II) complex, featuring a typical spin-interconversion behavior.[29] It had four non-equivalent imidazole and pyrazole sites, exhibiting five switchable electronic states with different ligand-field strength by sequential deprotonation steps. Very recently, such multilevel proton-induced magnetic response has also been achieved in an air-stable cubic Fe_8^{III} metal–organic cage with twelve monodeprotonated bis-bidentate ligands, 2,2′-(1*H*-imidazole-4,5-diyl)bis(1,4,5,6-tetrahydropyrimidine), as edges, which affords 12 switchable spin states *via* precise deprotonation and protonation at the NH active sites of the ligands.[30] However, we notice that the above acid–base controls were all carried out in solution, which somewhat hinders the deep understanding of their structure–property-function relationships.

Herein, we report an Et_3N- or chiral amine-triggered SC–SC transformation in a mononuclear Fe(II) complex, $[Fe(H_2L)_2](BF_4)_2$ [H_2L = 4-iodo-2,6-di(1*H*-imidazole-2-yl)pyridine] (**Fe-BF$_4$**), *via* the deprotonation of the NH sites in the imidazole motif (Scheme 1). The imidazole moieties and terminal iodo groups were strategically incorporated to facilitate the formation of extensive N–H···N hydrogen bonds and C–I···N halogen bonds, which were anticipated to simultaneously maintain crystallinity and direct the supramolecular framework topology.[17,31] We initially investigated Et_3N serving as a proton abstractor to mediate the SC–SC transformation of **Fe-BF$_4$**. Interestingly, when excess Et_3N was employed, the system underwent conversion to $[Fe(L)_2][Et_3NH]$, which adopted a 1D chain topology stabilized by halogen bonding. This observation prompted us to explore chiral amines for constructing topologically chiral architectures. Remarkably, employing optically pure *R*/*S*-quinuclidinol as a chiral inducer enabled a four-stage hierarchical assembly process, ultimately yielding enantiomeric 3D frameworks with three-fold interpenetration.

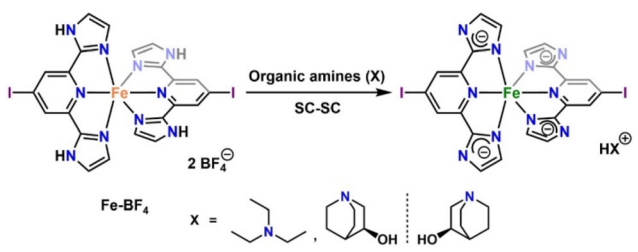

Scheme 1 SC–SC transformation protocol of **Fe-BF$_4$**.

Moreover, the above transformations were accompanied by a switch in spin states.

Results and discussion

Fe-BF$_4$ was prepared by a room-temperature solution reaction between H_2L and $Fe(BF_4)_2{\cdot}6H_2O$ in a molar ratio of 2 : 1 in CH_3CN. The solid structure of **Fe-BF$_4$** was determined by single-crystal X-ray diffraction (SC-XRD) at room temperature and is displayed in Fig. 1. The compound crystallized in the orthorhombic space group *Pbcn* (Table S1), consisting of two H_2L, one Fe(II) ion and two BF_4^- ions as non-coordinating counterions. The Fe(II) center coordinated with six nitrogen atoms from two H_2L, forming a distorted octahedral coordination geometry. At 300 K, the Fe–N bond lengths ranged from 1.925(4) to 1.999(4) Å (Table S2), giving an average bond length of 1.971 Å. The average *trans* N(pyridine)–Fe–N(pyridine) angle ϕ and dihedral twist angle θ [21,32] were 178.79 and 88.01°, respectively (Table S2). When the temperature was increased to 400 K, the space group remained unchanged, but the unit cell volume expanded from 2949.2 to 3028.1 Å (Table S1). Accordingly, the average length of Fe–N bonds increased from 1.971 to 2.117 Å, although ϕ and θ did not change much; ϕ = 178.39° and θ = 86.99° (Table S2). Notable changes in angular (Σ) and torsional (Θ) distortion parameters[21,33] were also observed: Σ(300 K) = 88.48°, Σ(400 K) = 124.73°, Θ(300 K) = 288.56° and Θ(400 K) = 402.91°. All the above changes implied a temperature-induced spin-crossover behavior in **Fe-BF$_4$**. The packing diagram of **Fe-BF$_4$** along the crystallographic *b* axis revealed that the counter anions BF_4^- acted as bridging units between the neighboring molecules, forming a 3D network *via* N–H···F interactions. This arrangement resulted in the shortest intermolecular Fe(II)···Fe(II) separation of 8.936 Å at 300 K (Fig. S1).

Given the acid/base response of the imidazole group, we investigated the acid–base interconversion of **Fe-BF$_4$** among different spin states. Firstly, Et_3N was reacted with the NH protons of the imidazole moiety, and it was found that the compound underwent SC–SC transformations accompanied by the oxidation of Fe(II) to Fe(III) (Fig. 1). It should be clarified that such an SC–SC transformation was not feasible under anaerobic conditions since oxygen, as established in the literature,[34,35] is essential for such oxidation. When three equivalents of Et_3N were used, **Fe-BF$_4$** was successfully transformed into a neutral Fe(III) complex, [Fe(HL)(L)] (**Fe-1H**), which contained three deprotonated and one protonated imidazole groups. Upon treatment with a large excess of Et_3N, four NH protons in **Fe-BF$_4$** were completely consumed, producing an Fe(III) anionic unit balanced by an $[Et_3NH]^+$ cation, $[Fe(L)_2]{\cdot}(Et_3NH){\cdot}H_2O$ (**Fe-Et$_3$N**). In addition, **Fe-1H** could be obtained by adding one equivalent of glacial acetic acid to **Fe-Et$_3$N** in an SC–SC transformation process. These transformations from Fe(II) to Fe(III) complexes were further confirmed by the disappearance of the peak centered at *ca.* 540 nm in the absorption spectra (metal-to-ligand charge transfer process,

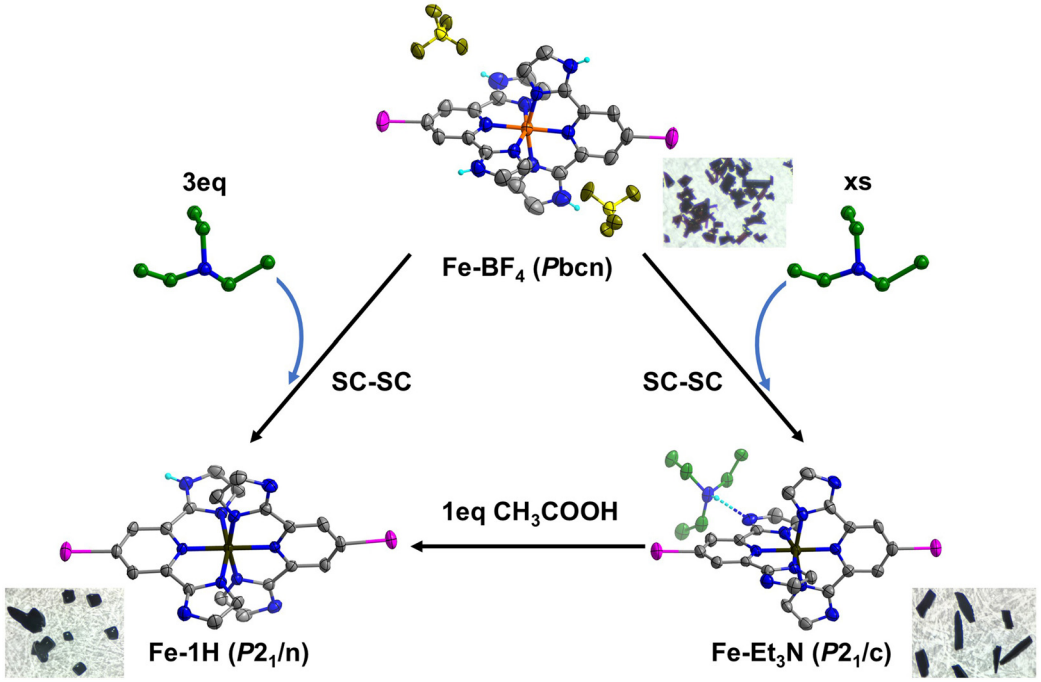

Fig. 1 Et_3N-driven SC–SC transformation of **Fe-BF_4**. Color codes: Fe(II)-orange, Fe(III)-black, N-blue, C in Fe(II)/Fe(III) units-gray, C in amine units-green, I-pink, B-yellow, F-dark yellow, and H-turquoise.

Fig. 2), the vanishing of a broad peak in the region within 25–40 ppm in the ^{1}H NMR spectra (intrinsic paramagnetism of Fe(II), Fig. S13 and S14), and the XPS data (Fig. S25 and S26). Moreover, it is worthy to note that the Fe(III) species could be converted back to the Fe(II) species by adding equivalent amounts of hydroxylamine hydrochloride in methanol, as confirmed by UV-Vis spectra, ^{1}H NMR spectra and magnetic measurements (Fig. S12, S15, S16 and S22). The single crystals of the above reductive compounds were obtained by slow diffusion of diethyl ether into a methanol solution. SC-XRD analysis revealed that all the reductive species were identical, named by **Fe-Re**. Its solid structure is shown in Fig. S9, and the structural details are presented in Tables S10–S12.

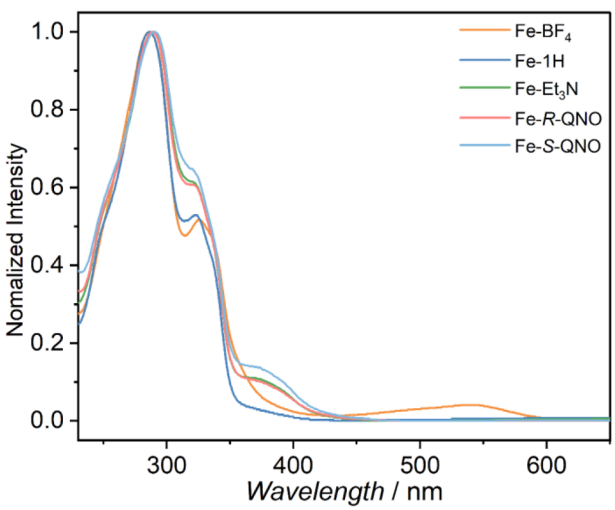

Fig. 2 UV-Vis absorption spectra of **Fe-BF_4**, **Fe-1H**, **Fe-Et_3N**, **Fe-*R*-QNO** and **Fe-*S*-QNO** in MeOH ($c = 10^{-5}$ M).

Compounds **Fe-1H** and **Fe-Et_3N** crystallized in the space groups of lower symmetry, $P2_1/n$ and $P2_1/c$, respectively, than **Fe-BF_4** (Table S4). The structural distortion of **Fe-1H** was smaller than that of **Fe-BF_4**, as demonstrated by its larger ϕ (179.00°) and θ(89.45°) and smaller Σ(75.97°) and Θ(249.61°) values (Table S5). In **Fe-1H**, adjacent molecules were connected by orthogonal N–H···N hydrogen bonding and C–I···N halogen bonding interactions, producing a 2D network structure (Fig. S3). In comparison, **Fe-Et_3N** possessed four deprotonated imidazole groups and an $[Et_3NH]^+$ for balancing the charge. The average length of Fe–N bonds and angles of ϕ and θ were 1.928 Å, 177.96°, and 88.85°, respectively (Table S5). Compared with **Fe-BF_4**, the Σ and Θ parameters of **Fe-Et_3N** reduced from 88.48° and 288.56° to 78.50° and 265.59°, respectively (Table S5). In contrast to **Fe-1H**, the topological supramolecular architecture of **Fe-Et_3N** was the C–I···N halogen-bonded 1D chain with discrete N–H···N hydrogen bonds between $[Et_3NH]^+$ and one deprotonated imidazole group (Fig. S5). The shortest intermolecular Fe(III)···Fe(III) distances for **Fe-1H** and **Fe-Et_3N** were 7.677 and 7.601 Å, respectively (Fig. S2 and S4).

The magnetic susceptibilities of the above three compounds were measured under a 1000 Oe direct current magnetic field over the temperature range of 5–400 K. Thermogravimetric analysis (TGA) curves, as shown in Fig. S10, verified that they were all thermally stable at 400 K. **Fe-BF_4** exhibited an incomplete and gradual SCO behavior,

while the other two Fe(III) complexes, **Fe-1H** and **Fe-Et$_3$N**, showed the predominant low-spin state of Fe(III) across the entire temperature range, indicating that the amine-driven SC–SC transformation successfully induced a spin-state switch. As shown in the top panel of Fig. 3, the $\chi_M T$ value of **Fe-BF$_4$** at 400 K was 2.47 cm^3 K mol^{-1}, which corresponded to 82% of the high-spin state of Fe(II) (S = 2, g = 2).[30] As the temperature dropped, the $\chi_M T$ value showed a noticeable decline and reached 0.1 cm^3 K mol^{-1} at 224 K, suggesting an almost complete low-spin state of Fe(II) (S = 0, g = 2). For **Fe-1H** and **Fe-Et$_3$N**, the $\chi_M T$ values at 400 K were *ca.* 0.58 and 0.72 cm^3 K mol^{-1}, respectively, corresponding to the predominant low-spin state of Fe(III) (S = 1/2, g = 2). The larger $\chi_M T$ value in the latter implied that further deprotonation of the imidazole group may prompt the Fe(III) center to transition to the high-spin state.[30] Their $\chi_M T$ values did not change significantly with decreasing temperature, demonstrating the absence of SCO behavior in these two Fe(III) complexes. Furthermore, the magnetic signature of this low-spin state could revert to that of the SCO *via* reduction with hydroxylamine hydrochloride (Fig. S21). X-band EPR spectroscopy was also employed to further elucidate the spin state of the Fe(III) complexes following the SC–SC transition. Results for both **Fe-1H** and **Fe-Et$_3$N** revealed typical low-spin signals of Fe(III) complexes (S = 1/2) (middle and bottom panels of Fig. 3). Fitting the spectra yielded anisotropic g-tensors of g_x = 2.27, g_y = 2.26, g_z = 1.89 for **Fe-1H** and g_x = 2.24, g_y = 2.23, g_z = 1.91 for **Fe-Et$_3$N**. These values were similar to those of the previously reported low-spin Fe(III) complexes.[36,37]

Chiral amines serve as crucial structural motifs with broad applications across diverse fields, including drug preparation,[38–40] asymmetric catalysis,[41] and ferroelectric materials.[15] The successful incorporation of Et$_3$N into the lattice of **Fe-BF$_4$** prompted us to employ chiral amines to drive such transformations for obtaining intriguing chiral supramolecular organic frameworks supported by the hydrogen and/or halogen bonds. Herein, we used optically pure organic amines, *R*/*S*-quinuclidinol (*R*/*S*-QNO), to drive the SC-SC transformation of **Fe-BF$_4$**. When an excess of *R*/*S*-QNO was added, the color of the **Fe-BF$_4$** crystals gradually changed from crimson to black without the loss of crystallinity, yielding the homochiral Fe(III) complex, [Fe(L)$_2$]·(*R*/*S*-QNO-H)·3CH$_3$CN (**Fe-*R*/*S*-QNO**). This complex was characterized by SC-XRD, UV-Vis spectroscopy and ^{1}H NMR spectroscopy (Fig. 2, 4, S17 and S18). Note that this is a nonbonding method for chiral induction, *i.e.* the protonated chiral amines serve as inherent sources of chirality, showing hydrogen-bond interaction with the periphery of the Fe(III) coordination sphere. More importantly, the integration of [Fe(L)$_2$] (achiral "soldiers") and chiral organic amines (chiral "sergeants") *via* weak interactions achieved remote chirality transfer and effective chiral amplification (Fig. 4). The enantiomeric nature of **Fe-*R*-QNO** and **Fe-*S*-QNO** was unequivocally established by their mirror-symmetric crystal structures. For clarity, we focus our discussion on **Fe-*R*-QNO** as a representative example. SC-XRD revealed that **Fe-*R*-QNO** crystallized in the chiral space group $P2_12_12_1$ (Table S7).

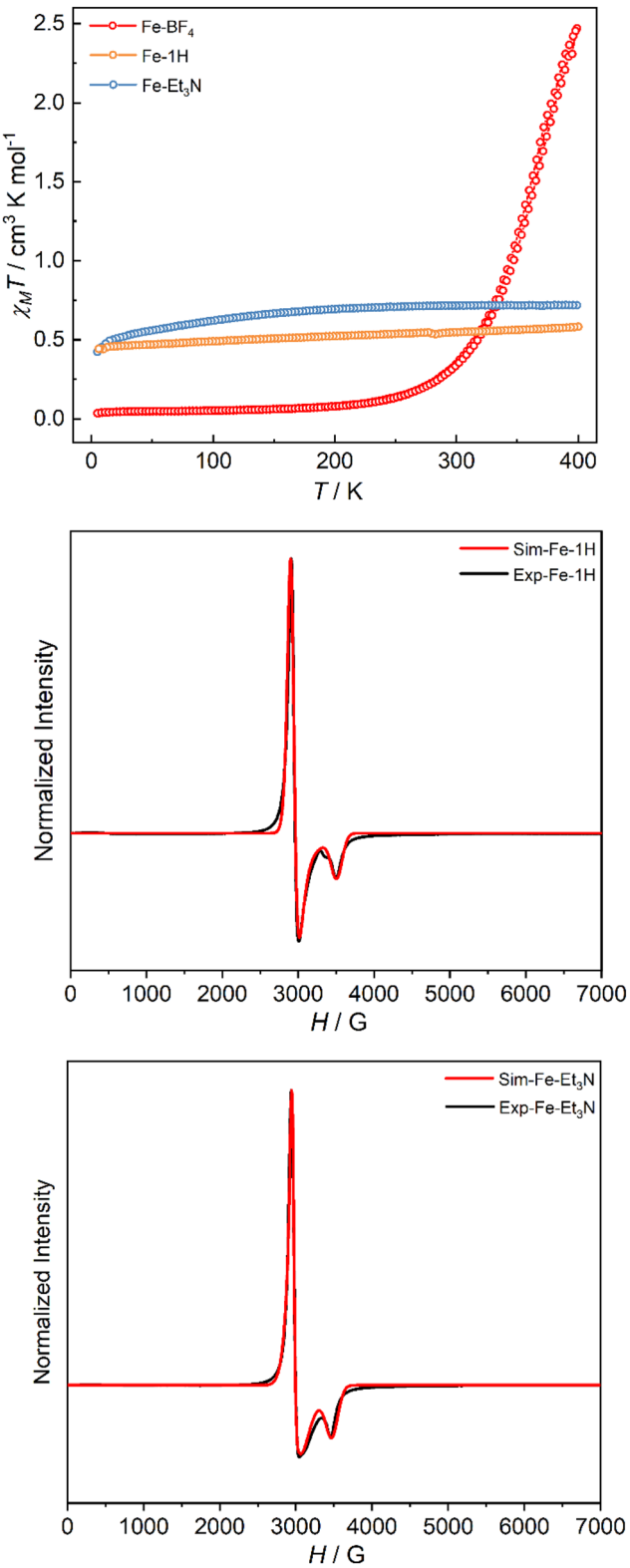

Fig. 3 Top: Temperature dependence of $\chi_M T$ values for **Fe-BF$_4$**, **Fe-1H** and **Fe-Et$_3$N**. Experimental and simulated EPR spectra of **Fe-1H** (middle) and **Fe-Et$_3$N** (bottom) at room temperature.

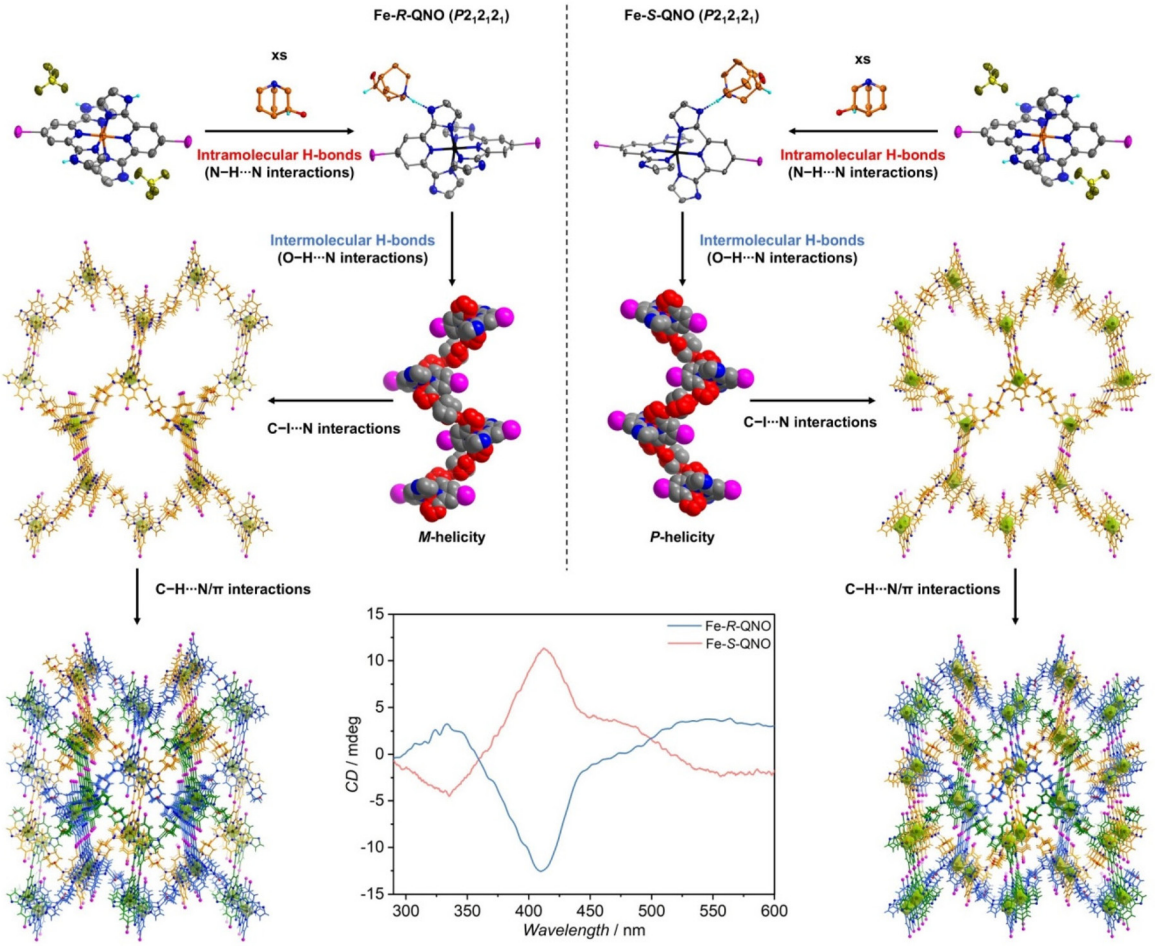

Fig. 4 Synthetic route, chiral superstructures and CD spectra of **Fe-*R*/*S*-QNO**. All solvents are omitted for clarity. Label: 1D hydrogen-bonded helical chains, space-filling model.

The asymmetric unit of **Fe-*R*-QNO** included one iron-centered anion, $[Fe(L)_2]^-$, one chiral amine cation, $[R\text{-QNO-H}]^+$, and three CH_3CN molecules (Fig. S6). Interestingly, the protonated amino group and –OH group of *R*-QNO simultaneously engaged in hydrogen bonding with $[Fe(L)_2]^-$ units, giving rise to a 1D hydrogen-bonded helical chain with *M*-helicity (Fig. 4 and S7). These 1D chains were further connected by the orthogonal C–I···N halogen bonds, giving three 3D hexagonal windows along the crystallographic *a* axis. Finally, these windows were held together in an alternating pattern *via* abundant C–H···π and C–H···N interactions between organic amines and imidazole motifs or two intermolecular imidazole motifs, forming a threefold interwoven topology (Fig. 4). Correspondingly, the supramolecular organic framework of **Fe-*S*-QNO** was constructed in the same hierarchical assembly as that of **Fe-*R*-QNO**. As shown in Fig. 4 and S8, each stage of the assembly of **Fe-*S*-QNO** resulted in a mirror-symmetric structure relative to that of **Fe-*R*-QNO**. Compared with the silent CD signal in solution (Fig. S19), the solid-state CD spectra exhibited the most intense signals at *ca.* 410 nm (Fig. 4), clearly demonstrating the successful transfer of chirality from the chiral amine cations to the supramolecular structure. Such an SC–SC transformation from centrosymmetric crystals to chiral crystals *via* the nonbonding approach provides an alternative for preparing chiral supramolecular organic frameworks, which is reminiscent of the combination of chiral amine drugs with proteins in living organisms. Additionally, this chiral amine-driven SC–SC transformation induced changes in magnetic properties, from SCO behavior to a low-spin Fe(III) state, as confirmed by the magnetic measurements and EPR spectra (Fig. S20, S21, S23 and S24).

Conclusions

In summary, we developed a mononuclear Fe(II) complex functionalized with acid–base-responsive imidazole moieties and terminal iodo groups that serves as a versatile building block for constructing achiral and chiral supramolecular architectures. These structures were obtained through a rare amine-driven SC–SC transformation process. In **Fe-1H**, a 2D supramolecular network was formed through the cooperative action of orthogonal intermolecular hydrogen and halogen bonds. In contrast, **Fe-Et$_3$N** adopted a 1D chain structure mediated by

halogen bonding, complemented by discrete intramolecular hydrogen bonds. Remarkably, when optically pure *R*/*S*-quinuclidinol was used, we observed a homochiral hydrogen-bonded helical 1D chain with *M*-/*P*-helicity. These helical chains were further interconnected through the orthogonal C–I···N halogen bonds, constructing a 3D chiral network that eventually packed into a three-fold interpenetrated framework *via* C–H···N/π interactions, achieving a four-stage chiral hierarchical assembly. Moreover, these SC–SC transformations induced corresponding changes in magnetic properties: from SCO behavior in parent **Fe-BF$_4$** to the low-spin state of Fe(III) complexes. This SC–SC transformation *via* nonbonding interactions paves a new way for the transfer and amplification of chirality and the modulation of topologies and spin states in supramolecular frameworks.

Author contributions

J. Tang conceived the idea. X. Ying, Z. Zhu and P. Xu performed the synthesis and characterization. Z. Zhu, X. Ying, J. Tang and Q. Zhou wrote the manuscript with contributions from all authors.

Conflicts of interest

There are no conflicts to declare.

Data availability

All data that support the conclusion of this study are available in this article and its supplementary information (SI). Supplementary information: synthetic procedures, single-crystal data, characterization and magnetic measurements. See DOI: **https://doi.org/10.1039/d5qi01812a**.

CCDC 2378478–2378481, 2378488, 2468133 and 2468134 contain the supplementary crystallographic data for this paper.[42a–g]

Acknowledgements

We thank the support from the National Natural Science Foundation of China (22201279 and 92261103), the Key Research Program of Frontier Sciences, CAS (ZDBS-LY-SLH023), and the Natural Science Foundation of Jilin Province State Key Laboratory Major Project (SKL202302037) for this work.

References

1 A. P. Katsoulidis, D. Antypov, G. F. S. Whitehead, E. J. Carrington, D. J. Adams, N. G. Berry, G. R. Darling, M. S. Dyer and M. J. Rosseinsky, Chemical control of structure and guest uptake by a conformationally mobile porous material, *Nature*, 2019, **565**, 213–217.

2 E. Fernandez-Bartolome, A. Martinez-Martinez, E. Resines-Urien, L. Piñeiro-Lopez and J. S. Costa, Reversible single-crystal-to-single-crystal transformations in coordination compounds induced by external stimuli, *Coord. Chem. Rev.*, 2022, **452**, 214281.

3 W.-F. Deng, Y.-X. Li, Y.-X. Zhao, J.-S. Hu, Z.-S. Yao and J. Tao, Inversion of Molecular Chirality Associated with Ferroelectric Switching in a High-Temperature Two-Dimensional Perovskite Ferroelectric, *J. Am. Chem. Soc.*, 2023, **145**, 5545–5552.

4 J. X. Hu, Q. Li, H. L. Zhu, Z. N. Gao, Q. Zhang, T. Liu and G. M. Wang, Achieving large thermal hysteresis in an anthracene-based manganese(II) complex via photo-induced electron transfer, *Nat. Commun.*, 2022, **13**, 2646.

5 Z. Zhu, X.-L. Li, S. Liu and J. Tang, External stimuli modulate the magnetic relaxation of lanthanide single-molecule magnets, *Inorg. Chem. Front.*, 2020, **7**, 3315–3326.

6 K. Morimoto, D. Kitagawa, H. Sotome, S. Ito, H. Miyasaka and S. Kobatake, Edge-to-Center Propagation of Photochemical Reaction during Single-Crystal-to-Single-Crystal Photomechanical Transformation of 2,5-Distyrylpyrazine Crystals, *Angew. Chem., Int. Ed.*, 2022, **61**, e202212290.

7 S. Bhandary, M. Beliš, A. M. Kaczmarek and K. Van Hecke, Photomechanical Motions in Organoboron-Based Phosphorescent Molecular Crystals Driven by a Crystal-State [2 + 2] Cycloaddition Reaction, *J. Am. Chem. Soc.*, 2022, **144**, 22051–22058.

8 C.-D. Wu and W. Lin, Highly Porous, Homochiral Metal–Organic Frameworks: Solvent-Exchange-Induced Single-Crystal to Single-Crystal Transformations, *Angew. Chem., Int. Ed.*, 2005, **44**, 1958–1961.

9 S. Kobatake, S. Takami, H. Muto, T. Ishikawa and M. Irie, Rapid and reversible shape changes of molecular crystals on photoirradiation, *Nature*, 2007, **446**, 778–781.

10 D. A. Sherman, R. Murase, S. G. Duyker, Q. Gu, W. Lewis, T. Lu, Y. Liu and D. M. D'Alessandro, Reversible single crystal-to-single crystal double [2+2] cycloaddition induces multifunctional photo-mechano-electrochemical properties in framework materials, *Nat. Commun.*, 2020, **11**, 2808.

11 M. Hojorat, H. Al Sabea, L. Norel, K. Bernot, T. Roisnel, F. Gendron, B. L. Guennic, E. Trzop, E. Collet, J. R. Long and S. Rigaut, Hysteresis Photomodulation via Single-Crystal-to-Single-Crystal Isomerization of a Photochromic Chain of Dysprosium Single-Molecule Magnets, *J. Am. Chem. Soc.*, 2020, **142**, 931–936.

12 J. Alfuth, O. Jeannin and M. Fourmigué, Topochemical, Single-Crystal-to-Single-Crystal [2+2] Photocycloadditions Driven by Chalcogen-Bonding Interactions, *Angew. Chem., Int. Ed.*, 2022, **61**, e202206249.

13 K. Staszak, K. Wieszczycka, V. Marturano and B. Tylkowski, Lanthanides complexes – Chiral sensing of biomolecules, *Coord. Chem. Rev.*, 2019, **397**, 76–90.

14 H.-Y. Wong, W.-S. Lo, K.-H. Yim and G.-L. Law, Chirality and Chiroptics of Lanthanide Molecular and Supramolecular Assemblies, *Chem*, 2019, **5**, 3058–3095.

15 H.-Y. Liu, H.-Y. Zhang, X.-G. Chen and R.-G. Xiong, Molecular Design Principles for Ferroelectrics: Ferroelectrochemistry, *J. Am. Chem. Soc.*, 2020, **142**, 15205–15218.
16 Y.-J. Zhang, T. Liu, S. Kanegawa and O. Sato, Reversible Single-Crystal-to-Single-Crystal Transformation from Achiral Antiferromagnetic Hexanuclears to a Chiral Ferrimagnetic Double Zigzag Chain, *J. Am. Chem. Soc.*, 2009, **131**, 7942–7943.
17 Y. Li, B. Zhao, J.-P. Xue, J. Xie, Z.-S. Yao and J. Tao, Giant single-crystal-to-single-crystal transformations associated with chiral interconversion induced by elimination of chelating ligands, *Nat. Commun.*, 2021, **12**, 6908.
18 S. Xue, Y. Guo and Y. Garcia, Spin crossover crystalline materials engineered via single-crystal-to-single-crystal transformations, *CrystEngComm*, 2021, **23**, 7899–7915.
19 Z.-Y. Li, J.-W. Dai, M. Damjanović, T. Shiga, J.-H. Wang, J. Zhao, H. Oshio, M. Yamashita and X.-H. Bu, Structure Switching and Modulation of the Magnetic Properties in Diarylethene-Bridged Metallosupramolecular Compounds by Controlled Coordination-Driven Self-Assembly, *Angew. Chem., Int. Ed.*, 2019, **58**, 4339–4344.
20 J. S. Costa, S. Rodríguez-Jiménez, G. A. Craig, B. Barth, C. M. Beavers, S. J. Teat and G. Aromí, Three-Way Crystal-to-Crystal Reversible Transformation and Controlled Spin Switching by a Nonporous Molecular Material, *J. Am. Chem. Soc.*, 2014, **136**, 3869–3874.
21 M. A. Halcrow, Structure:function relationships in molecular spin-crossover complexes, *Chem. Soc. Rev.*, 2011, **40**, 4119–4142.
22 Y.-T. Wang, S.-T. Li, S.-Q. Wu, A.-L. Cui, D.-Z. Shen and H.-Z. Kou, Spin Transitions in Fe(II) Metallogrids Modulated by Substituents, Counteranions, and Solvents, *J. Am. Chem. Soc.*, 2013, **135**, 5942–5945.
23 D. Shao, L. Shi, F.-X. Shen, X.-Q. Wei, O. Sato and X.-Y. Wang, Reversible On–Off Switching of the Hysteretic Spin Crossover in a Cobalt(II) Complex via Crystal to Crystal Transformation, *Inorg. Chem.*, 2019, **58**, 11589–11598.
24 X.-D. Huang, Y. Xu, K. Fan, S.-S. Bao, M. Kurmoo and L.-M. Zheng, Reversible SC-SC Transformation involving [4+4] Cycloaddition of Anthracene: A Single-Ion to Single-Molecule Magnet and Yellow-Green to Blue-White Emission, *Angew. Chem., Int. Ed.*, 2018, **57**, 8577–8581.
25 R. Rabelo, L. Toma, N. Moliner, M. Julve, F. Lloret, M. Inclán, E. García-España, J. Pasán, R. Ruiz-García and J. Cano, pH-Switching of the luminescent, redox, and magnetic properties in a spin crossover cobalt(II) molecular nanomagnet, *Chem. Sci.*, 2023, **14**, 8850–8859.
26 P. Su, B. Wei, C. Guo, Y. Hu, R. Tang, S. Zhang, C. He, J. Lin, X. Yu, Z. Chen, H. Li, H. Wang and X. Li, Metallo-Supramolecular Hexagonal Wreath with Four Switchable States Based on a pH-Responsive Tridentate Ligand, *J. Am. Chem. Soc.*, 2023, **145**, 3131–3145.
27 R. Nowak, E. A. Prasetyanto, L. De Cola, B. Bojer, R. Siegel, J. Senker, E. Rössler and B. Weber, Proton-driven coordination-induced spin state switch (PD-CISSS) of iron(II) complexes, *Chem. Commun.*, 2017, **53**, 971–974.
28 S. Dhers, A. Mondal, D. Aguilà, J. Ramírez, S. Vela, P. Dechambenoit, M. Rouzières, J. R. Nitschke, R. Clérac and J.-M. Lehn, Spin State Chemistry: Modulation of Ligand pKa by Spin State Switching in a [2×2] Iron(II) Grid-Type Complex, *J. Am. Chem. Soc.*, 2018, **140**, 8218–8227.
29 T. Shiga, R. Saiki, L. Akiyama, R. Kumai, D. Natke, F. Renz, J. M. Cameron, G. N. Newton and H. Oshio, A Brønsted-Ligand-Based Iron Complex as a Molecular Switch with Five Accessible States, *Angew. Chem., Int. Ed.*, 2019, **58**, 5658–5662.
30 Z.-K. Liu, X.-Y. Ji, M. Yu, Y.-X. Li, J.-S. Hu, Y.-M. Zhao, Z.-S. Yao and J. Tao, Proton-Induced Reversible Spin-State Switching in Octanuclear FeIII Spin-Crossover Metal–Organic Cages, *J. Am. Chem. Soc.*, 2024, **146**, 22036–22046.
31 T. Itoh, S. Nomura, H. Nakasho, T. Uno, M. Kubo, N. Tohnai and M. Miyata, Halogen Bond Effect for Single-Crystal-to-Single-Crystal Transformation: Topochemical Polymerization of Substituted Quinodimethane, *Macromolecules*, 2015, **48**, 5450–5455.
32 Q. Yang, Y.-S. Meng, T. Liu and J. Tang, Thermal and photoinduced spin-crossover of mononuclear FeII complexes based on bppCHO ligand, *Dalton Trans.*, 2022, **51**, 602–607.
33 R. Ketkaew, Y. Tantirungrotechai, P. Harding, G. Chastanet, P. Guionneau, M. Marchivie and D. J. Harding, OctaDist: a tool for calculating distortion parameters in spin crossover and coordination complexes, *Dalton Trans.*, 2021, **50**, 1086–1096.
34 R. F. Carina, L. Verzegnassi, A. F. Williams and G. Bernardinelli, Modulation of iron reduction potential by deprotonation at a remote site, *Chem. Commun.*, 1998, 2681–2682.
35 G. Stupka, L. Gremaud, G. Bernardinelli and A. F. Williams, Redox state switching of transition metals by deprotonation of the tridentate ligand 2,6-bis(imidazol-2-yl)pyridine, *Dalton Trans.*, 2004, 407–412.
36 S.-C. Chan, P. Gupta, X. Engelmann, Z. Z. Ang, R. Ganguly, E. Bill, K. Ray, S. Ye and J. England, Observation of Carbodicarbene Ligand Redox Noninnocence in Highly Oxidized Iron Complexes, *Angew. Chem., Int. Ed.*, 2018, **57**, 15717–15722.
37 N. E. Domracheva, A. V. Pyataev, V. E. Vorobeva and E. M. Zueva, Detailed EPR Study of Spin Crossover Dendrimeric Iron(III) Complex, *J. Phys. Chem. B*, 2013, **117**, 7833–7842.
38 A. Calcaterra and I. D'Acquarica, The market of chiral drugs: Chiral switches versus de novo enantiomerically pure compounds, *J. Pharm. Biomed. Anal.*, 2018, **147**, 323–340.
39 A. Cabré, X. Verdaguer and A. Riera, Recent Advances in the Enantioselective Synthesis of Chiral Amines via Transition Metal-Catalyzed Asymmetric Hydrogenation, *Chem. Rev.*, 2022, **122**, 269–339.
40 Z.-Y. Zhu, M. Shi, C.-L. Li, Y.-F. Gao, X.-Y. Shen, X.-W. Ding, F.-F. Chen, J.-H. Xu, Q. Chen and G.-W. Zheng, An

Engineered Imine Reductase for Highly Diastereo- and Enantioselective Synthesis of β-Branched Amines with Contiguous Stereocenters, *Angew. Chem., Int. Ed.*, 2024, **63**, e202408686.

41 Y. Xu, Q. Sun, T.-D. Tan, M.-Y. Yang, P. Yuan, S.-Q. Wu, X. Lu, X. Hong and L.-W. Ye, Organocatalytic Enantioselective Conia-Ene-Type Carbocyclization of Ynamide Cyclohexanones: Regiodivergent Synthesis of Morphans and Normorphans, *Angew. Chem., Int. Ed.*, 2019, **58**, 16252–16259.

42 (*a*) CCDC 2378478: Experimental Crystal Structure Determination, 2025, DOI: **10.5517/ccdc.csd.cc2kv03k**; (*b*) CCDC 2378479: Experimental Crystal Structure Determination, 2025, DOI: **10.5517/ccdc.csd.cc2kv04l**; (*c*) CCDC 2378480: Experimental Crystal Structure Determination, 2025, DOI: **10.5517/ccdc.csd.cc2kv05m**; (*d*) CCDC 2378481: Experimental Crystal Structure Determination, 2025, DOI: **10.5517/ccdc.csd.cc2kv06n**; (*e*) CCDC 2378488: Experimental Crystal Structure Determination, 2025, DOI: **10.5517/ccdc.csd.cc2kv0fw**; (*f*) CCDC 2468133: Experimental Crystal Structure Determination, 2025, DOI: **10.5517/ccdc.csd.cc2nv961**; (*g*) CCDC 2468134: Experimental Crystal Structure Determination, 2025, DOI: **10.5517/ccdc.csd.cc2nv972**.